

Sideband pump-probe technique resolves nonlinear modulation response of PbS/CdS quantum dots on a silicon nitride waveguide

Mirco Kolarczik, Christian Ulbrich, Pieter Geiregat, Yunpeng Zhu, Laxmi Kishore Sagar, Akshay Singh, Bastian Herzog, Alexander W. Achtstein, Xiaoqin Li, Dries van Thourhout, Zeger Hens, Nina Owschimikow, and Ulrike Woggon

Citation: *APL Photonics* **3**, 016101 (2018);

View online: <https://doi.org/10.1063/1.5005490>

View Table of Contents: <http://aip.scitation.org/toc/app/3/1>

Published by the [American Institute of Physics](#)

Articles you may be interested in

[Single-photon detectors combining high efficiency, high detection rates, and ultra-high timing resolution](#)
APL Photonics **2**, 111301 (2017); 10.1063/1.5000001

[Interferometric control of the photon-number distribution](#)
APL Photonics **2**, 071301 (2017); 10.1063/1.4992018

[Negative force on free carriers in positive index nanoparticles](#)
APL Photonics **2**, 101301 (2017); 10.1063/1.4991567

[Nanodiamonds with photostable, sub-gigahertz linewidth quantum emitters](#)
APL Photonics **2**, 116103 (2017); 10.1063/1.4998199



STEM CAREER WEBINARS
on networking, interviewing, conferences, presenting...

AIP
American Institute of Physics

www.physicstoday.org/jobs/webinars

The banner features a yellow background with a series of overlapping speech bubbles in various colors (green, blue, purple, red) containing white icons representing different STEM fields: a microscope, a graduation cap, an atom, a test tube rack, a molecular structure, and a flask. The AIP logo is prominently displayed in a green bubble on the left.

Sideband pump-probe technique resolves nonlinear modulation response of PbS/CdS quantum dots on a silicon nitride waveguide

Mirco Kolarczik,^{1,a} Christian Ulbrich,¹ Pieter Geiregat,^{2,3} Yunpeng Zhu,³ Laxmi Kishore Sagar,² Akshay Singh,^{4,b} Bastian Herzog,¹ Alexander W. Achtstein,¹ Xiaoqin Li,^{4,b} Dries van Thourhout,³ Zeger Hens,² Nina Owschimikow,^{1,c} and Ulrike Woggon¹

¹*Institut für Optik und Atomare Physik, Technische Universität Berlin, Berlin, Germany*

²*Department of Inorganic and Physical Chemistry, Ghent University, Ghent, Belgium*

³*Department of Information Technology, Ghent University, Ghent, Belgium*

⁴*Physics Department, University of Texas, Austin 78712, Texas, USA*

(Received 18 September 2017; accepted 22 November 2017;
published online 12 December 2017)

For possible applications of colloidal nanocrystals in optoelectronics and nanophotonics, it is of high interest to study their response at low excitation intensity with high repetition rates, as switching energies in the pJ/bit to sub-pJ/bit range are targeted. We develop a sensitive pump-probe method to study the carrier dynamics in colloidal PbS/CdS quantum dots deposited on a silicon nitride waveguide after excitation by laser pulses with an average energy of few pJ/pulse. We combine an amplitude modulation of the pump pulse with phase-sensitive heterodyne detection. This approach permits to use co-linearly propagating co-polarized pulses. The method allows resolving transmission changes of the order of 10^{-5} and phase changes of arcseconds. We find a modulation on a sub-nanosecond time scale caused by Auger processes and biexciton decay in the quantum dots. With ground state lifetimes exceeding $1 \mu\text{s}$, these processes become important for possible realizations of opto-electronic switching and modulation based on colloidal quantum dots emitting in the telecommunication wavelength regime. © 2017 Author(s). All article content, except where otherwise noted, is licensed under a Creative Commons Attribution (CC BY) license (<http://creativecommons.org/licenses/by/4.0/>). <https://doi.org/10.1063/1.5005490>

INTRODUCTION

In small semiconductor nanocrystals or quantum dots (QDs), the optical transition energy of an exciton is determined by the dimensions of the crystallite rather than the bandgap of the bulk material.^{1–4} This tunability, their long coherence lifetime,^{5,6} and the relatively low cost and scalability of the wet-chemical production, i.e., vacuum-free deposition methods such as spincoating, make colloidal QDs an attractive choice as active medium in photonic applications.^{7,8} Based on a variety of different material systems, light emitting devices and lasers have been fabricated using colloidal nanocrystals, recently even on chip.^{9–13}

As photonic devices mature, energy efficiency is becoming increasingly important. Currently, switching a bit with pulse powers in the few pJ range is a minimum requirement, and efforts are being made to enhance the power efficiency to reach the fJ/bit regime.^{14–16} To optimize and design colloidal nanocrystals for these applications, it is prerequisite to gain insight into the dynamical processes that are initiated by an optical excitation, in particular, for all-optical switching and

^aElectronic mail: mirco.kolarczik@tu-berlin.de

^bPresent address: Department of Material Science and Engineering, Massachusetts Institute of Technology, Cambridge, MA 02139, USA.

^cElectronic mail: nina.owschimikow@physik.tu-berlin.de



wavelength conversion processes. It is particularly important to understand differences and similarities in the response of the nanocrystals to a train of low power laser pulses at high repetition rates and the response to intense pulses with the same average power but much larger temporal spacing.

PbS and PbS/CdS colloidal QDs are particularly interesting for photonic and opto-electronic applications as their emission wavelength is tunable from 900 nm to 2000 nm, covering all relevant telecommunication windows.³ An important branch of photonics is the all-optical signal amplification and modulation. Opto-electronics is currently largely based on solid-state semiconductor sources using III-V semiconductors, for which exciton lifetimes are much shorter than the data transmission rates.¹⁷ In order for systems based on colloidal QDs to compete with the established technology, data rates are required to lie in the Gbit/s range, corresponding to one bit per 10^{-9} s. Colloidal QDs display ultrafast dynamics; however, most of the studies dedicated to these processes have been performed using amplified laser systems with a kHz repetition rate. An important aspect that needs consideration is the long lifetime of the exciton ground state in colloidal QDs, exceeding this time by up to three orders of magnitude.³ A fast data manipulation mechanism therefore needs to be based on an efficient nonlinear process,^{18,19} or the ground state (GS) lifetime has to be dramatically reduced. Colloidal QDs display large and size-tunable nonlinearities,^{20–22} of which, in particular, the efficient exciton multiplication has received considerable attention due to its potential impact on QD-based solar cells.^{23,24} For all-optical signal conversion, the relevant processes are, in particular, fast multi-exciton scattering events. A competing process is efficient broadband intraband absorption, which has been observed in pump-probe experiments.²⁵ Recently, it has been demonstrated that the effect of intra- and interband processes cancels at a specific wavelength, making ultrafast switching operations based on nonlinear interaction possible.¹⁹

In this contribution, we investigate the processes governing the modulation response of colloidal PbS/CdS core-shell^{4,26} QDs under a low power pulsed laser excitation with a high repetition rate. To obtain detectable signals, we maximize the interaction length between pump and probe pulses and the QDs by depositing the QDs onto a waveguide. In addition, we enhance the sensitivity of the detection by combining the advantages of a heterodyne-detected pump-probe experiment with the resolution of the double-chop approach. This combination allows us not only to detect changes in the transmission of the order of 10^{-5} but is also sensitive to phase changes of the same order, corresponding to arcseconds in absolute units.

SAMPLES

PbS QDs of 4.2 nm size (1200 nm emission wavelength) were prepared by following the procedure of Hendricks *et al.* published in Ref. 27. Pb-oleate was prepared by heating PbO (1 mol), oleic acid (2.1 mol), and dodecane at 125 °C under vacuum. For the synthesis of PbS QDs, in a nitrogen filled atmosphere, Pb-oleate (0.6 mmol) was taken in 9 ml of dodecane and flushed at 110 °C for 60 min. After that, reaction temperature was set to 95 °C and N, N'-diphenylthiourea (0.2 mmol) in 0.5 ml of diglyme was injected. After 3 min, the reaction was quenched with a water bath. The QDs were purified 2 times with toluene, methanol/isopropanol as solvent/non-solvent combination. PbS/CdS core/shell QDs were synthesized starting from 4.2 nm PbS core QDs by means of a cation exchange method, initially proposed by Pietryga *et al.* in Ref. 28. In a nitrogen-filled atmosphere, cadmium oleate was added in an atomic ratio of Cd:Pb = 10:1 to a PbS QD suspension in toluene. The reaction was quenched by the addition of methanol and butanol (1:2), and the QDs were purified two more times. This reaction typically gives a shell thickness of 1.1 nm.

The QDs are deposited by spin-coating on top of a chip with silicon nitride waveguides. Silicon and silicon nitride are important platforms in nanophotonics, promising the realization of chip-sized devices based on a CMOS-compatible fabrication technology.²⁹ Silicon nitride (Si_3N_4) can be manufactured into high quality low-loss waveguides and resonators.^{30–32} Additionally, a range of hybrid photonic devices based on silicon nitride structures has been demonstrated.^{10,33–37} In contrast to pure silicon, the material does not display large intrinsic nonlinearities or a substantial free carrier absorption³⁸ and therefore allows us to observe the nonlinear response of the QDs without

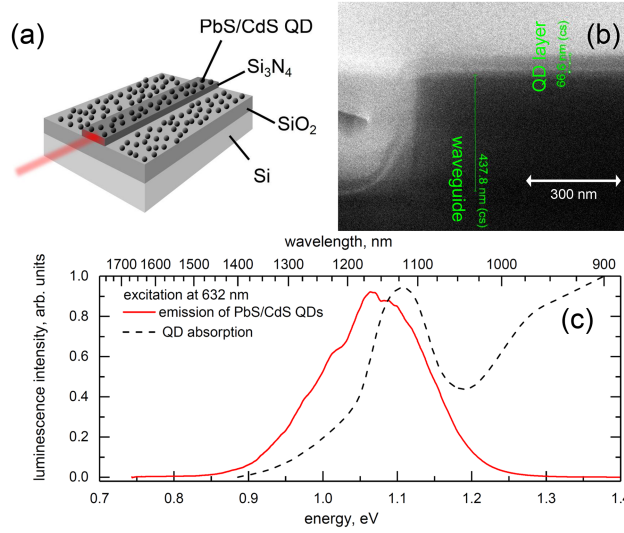


FIG. 1. (a) Schematic of the sample. (b) Scanning electron microscope image of the sample (sideview). (c) Room temperature photoluminescence spectrum (solid red line) of the PbS/CdS QDs. The excitation is by a HeNe laser. The dashed black line is an estimated QD absorption spectrum from the amplitudes of the pump-probe curves.

waveguide-induced background. A schematic of the sample is displayed in Fig. 1(a). Figure 1(b) shows a scanning electron microscope image of a facet of the sample. The spin-coated film containing QDs is clearly visible on top of the waveguide and has a thickness of about 66 nm. The sub-wavelength thickness ensures a good coupling to the optical mode.³⁹ The emission of the QDs upon excitation to the continuum states by means of a helium-neon laser and an estimated absorption spectrum based on the amplitude of the pump-probe curves are shown in Fig. 1(c).

SIDEBAND PUMP-PROBE EXPERIMENT

Heterodyne-detected pump-probe spectroscopy is a powerful tool to study dynamics in waveguide structures that require co-linear and co-polarized beam geometry.^{40,41} As a consequence of the co-linear propagation, probe pulse, pump pulse, and any additional light emitted from the waveguide overlap on the detector. To separate the probe pulse from the background intensity if, e.g., a spectral separation is not feasible, in a heterodyne-detected experiment, a frequency shift ν_1 is imposed onto the first order diffracted beam (the probe beam) by an acousto-optic modulator (AOM). This frequency shift acts as a marker that makes the probe pulse unique and distinguishable from all other detected radiation. When the frequency-shifted probe pulse is interfered with the unshifted original pulse (the so-called reference pulse), the marker frequency appears in the detected signal as a beat. As the laser modes are separated by the laser repetition rate $\nu_{\text{rep}} = 75.4$ MHz, the lowest beat frequency $\nu'_1 = \nu_1 - \nu_{\text{rep}}$ is detected by a lock-in amplifier as complex-valued signal $S \propto \mathcal{E}_{\text{ref}} \mathcal{E}_{\text{probe}}$, where \mathcal{E}_{ref} and $\mathcal{E}_{\text{probe}}$ are the electric fields of the reference and probe pulses, respectively.

Any pump-probe technique aims to detect a modification of $\mathcal{E}_{\text{probe}}(P) = \mathcal{E}_{\text{probe},0} \times \exp[(g(P) + i\phi(P))L]$ corresponding to the influence of a pump pulse of power P after the propagation length L . Due to the interferometric detection, a heterodyne-detected pump-probe experiment is not only able to measure the field gain coefficient g but also a phase coefficient ϕ corresponding to the refractive index n . In the classical heterodyne pump-probe scheme, the pump pulse is switched on and off sequentially to realize a differential measurement. The signals $S(P)$ with the pump pulse on and $S(0)$ with the pump pulse off are acquired, and the differential pump-probe signal is calculated from this pair of values as

$$\ln \frac{S(P)}{S(0)} = [(g(P) - g(0)) + i(\phi(P) - \phi(0))] L = \Delta G(P) + i\Delta\Phi(P). \quad (1)$$

Here, ΔG is referred to as the differential gain and $\Delta\Phi$ is referred to as the differential phase. To resolve independent subsequent values under switching of P , the signal recording period must exceed the chosen lock-in time constant (TC), as it is known from the sampling theorem. For $\nu'_1 > 1$ MHz and a small TC (1 μ s–10 μ s), remarkably high pump switching rates of tens of kilohertz are achievable, beyond the frequency range of acoustic and thermal noise. Apart from the very fast data acquisition, this scheme also offers the option of simultaneous multi-power measurements⁴¹ (SMPM), i.e., periodical alteration of the pump pulse power P in the sequential acquisition. As a drawback, small signals are obscured by noise if $S(P) \approx S(0)$.

An alternative scheme with significantly increased sensitivity is the double-chop detection approach. There, sinusoidal amplitude modulations are imprinted onto pump and probe pulse powers, and the lock-in detection is set to the beating of both frequencies, thus ensuring that modifications resulting from drifts of the pump pulse power are rejected. However, there are two major drawbacks in this traditional pump-probe technique: First, the standard double-chop technique does not implement a reference pulse which inhibits the measurement of the refractive index n . Second, the pump and probe laser modes are not frequency-shifted and therefore not distinguishable, resulting in undesired “probe-pump” signals at negative delay times.

For the experiments presented here, we retain the phase-sensitive heterodyne detection and replace the discrete switching of P by an additional fast amplitude modulation of the pump by the pump AOM at a modulation frequency $2\tilde{\nu}_2$. A second lock-in amplifier can be used to track the sideband of the heterodyne signal that originates from the pump amplitude modulation. Such usage of parallel lock-in amplifiers has been demonstrated for four-wave-mixing⁴² as well as pump-probe experiments.⁴³ Compared to Ref. 43, where mechanical choppers are used, fast modulation by an AOM yields a greatly improved separability of the relevant frequency bands which allows us to suppress strong bands by analog filtering (this signal pre-conditioning is the first and major key to small signal detection). Just as ν_1 acts as a marker of the probe pulse, $2\tilde{\nu}_2$ is a marker that is unique to the pump beam. When the sample mediates a pump-induced modification of the probe pulse, the probe pulse carries both markers, ν_1 and $2\tilde{\nu}_2$, respectively. In the frequency domain, this is represented by sidebands of ν'_1 appearing at $\nu'_1 \pm 2\tilde{\nu}_2$. With the second lock-in amplifier, one of these sidebands can be detected independently from the heterodyne lock-in signal S . The second sideband does not contain additional information, as the probe pulse response is always in phase with the comparatively slow modulation $2\tilde{\nu}_2$. For small signals $S(P) \approx S(0)$, the left hand side of Eq. (1) can be approximated by

$$\ln \frac{S(P)}{S(0)} \approx \frac{S(P)}{S(0)} - 1 = \frac{S(P) - S(0)}{S(0)} = \frac{\Delta S(P)}{S(0)}, \quad (2)$$

where ΔS represents the sideband lock-in signal. Because the TC of both lock-in amplifiers can be chosen in the range of 100 μ s–100 ms (large enough to separate both bands), the noise suppression is significantly enhanced, which is the second key to small signal detection. Our approach thus combines the superior sensitivity of a double-chop approach with the phase-sensitivity and the ability of co-linear/co-polarized geometry of heterodyne detection.

The setup is schematically displayed in Fig. 2(a). From the two independently tunable supercontinua of a Toptica FemtoFiber Pro SCIR laser system, pump and probe pulses are spectrally shaped in the Fourier plane of two pulse shapers to a spectral full width at half maximum of 15 nm and a pulse duration of ~ 300 fs. The pulses are detected by a New Focus Model 2117 detector in a balanced detection scheme for noise suppression. Instead of two fully independent lock-in amplifiers, we use a Zurich Instruments HF2LI with two independent demodulators. The first demodulator locks to the external reference ν'_1 by a phase-locked loop (PLL). The lock-in amplifier also generates the modulation frequency $\tilde{\nu}_2$. Due to the quadratic AOM response function [Fig. 2(b)], the lock-in output frequency $\tilde{\nu}_2$, if applied to the AOM driver, results in an amplitude modulation at $2\tilde{\nu}_2$. Deviations from the parabolic behavior for high modulation voltages generate undesired higher frequency components [Fig. 2(c)] that result in a non-sinusoidal temporal pump pulse modulation [Fig. 2(d)]. The second demodulator tracks the signal at $\nu'_1 - 2\tilde{\nu}_2$. The spectral position of main band and sideband is chosen according to the following signal conditioning requirements: The main band is placed at $\nu'_1 = 2$ MHz and with $\tilde{\nu}_2 = 975$ kHz, the sideband is located at $\nu'_1 - 2\tilde{\nu}_2 = 50$ kHz. The

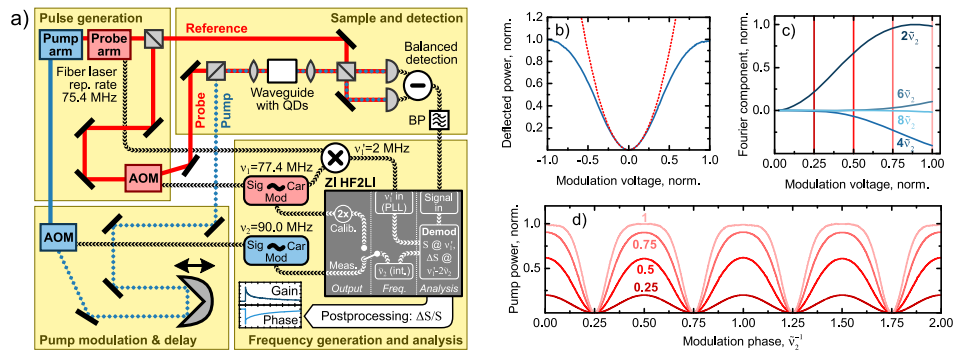


FIG. 2. (a) Experimental setup. (b) The modulation voltage scales the AOM carrier signal and results in a deflected power dependency (solid blue) that is parabolic (red dots) for small voltages. (c) The deviation from the parabolic behavior results in higher frequency components appearing for high modulation voltages. (d) The pulse train in the time domain calculated from the AOM behavior in (b) for the four different modulation voltages indicated by vertical lines in (c).

large absolute frequency difference $2\bar{\nu}_2$ allows for small TCs and therefore fast data acquisition. We set the low-pass filter of the detector to a cut-off frequency of 100 MHz to suppress the main band. For the analog pre-conditioning by a low-pass filter, the large frequency ratio $\nu'_1/(\nu'_1 - 2\bar{\nu}_2) = 40$ is crucial.

Although the two lock-in signals have a defined phase relation, the measured raw phase difference $\Delta\varphi$ still includes analog filter phase shifts. A calibration measurement is necessary to determine $\Delta\varphi_0$ for the case $\Delta G > 0$ and $\Delta\Phi = 0$. By applying the modulation frequency to the probe frequency generator, a pure amplitude modulation of the probe pulse is generated that is in phase with the internal frequency $2\bar{\nu}_2$. The resulting phase difference of this calibration measurement defines $\Delta\varphi_0$.

In a pump-probe experiment, in particular, at low pump pulse power, the phase changes one can expect are very small. Exploiting the fact that pump and probe pulses are coerced to propagate colinearly in a waveguide, the heterodyne detected pump-probe approach can yield an enhanced signal-to-noise ratio compared to a spatial pulse overlap only in the focal spot, as the signal is accumulated over the whole pump and probe propagation length. For low-loss waveguides, like the silicon nitride waveguides we employ,³⁶ the propagation length can reach macroscopic distances, as is exemplified in Fig. 3(a), where we show a top image of a blank silicon nitride waveguide with in- and outcoupling spots of our pilot laser. If waveguides are used to improve the pump-probe signal, care has to be taken, however, to ensure that both pump and probe pulses propagate in the same waveguide mode. This is an issue, in particular, in experiments with different colors of pump and probe pulses. Figure 3(b) shows an image of the outcoupling facet of a typical silicon nitride waveguide, where a pilot laser at 1120 nm propagates in the TE_{00} mode (left image) and in the TE_{01} mode (right image), depending on the incoupling angle. Obviously, the spatial overlap between two beams propagating in the two modes is massively reduced. As higher order modes also suffer from a temporal mode dispersion, it is important also to track the optimal temporal overlap of the pump and probe pulses. In our experiments, we used 4 μm wide waveguides, which

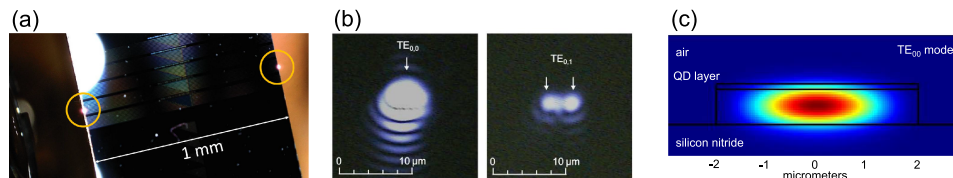


FIG. 3. (a) Top image of the chip. Laser spots at the in- and outcoupling facets of the silicon nitride waveguides are marked by yellow circles. In-coupling was performed via free-space optics; the short-focus lens is visible on the left hand side. (b) Images of the outcoupling facet, left: TE_{00} mode, right: TE_{01} mode. (c) Calculation of the mode profile.

become single-mode at wavelengths longer than 1200 nm. When using shorter pump wavelengths, we adjusted the incoupling angle such as to predominantly excite the TE_{00} mode for the pump pulse.

Figure 3(c) shows a calculation of the intensity profile of the TE_{00} mode propagating in a $4\ \mu\text{m}$ wide and 400 nm high silicon nitride waveguide covered with a 60 nm thick layer of PbS/CdS QDs, as deduced from the scanning electron microscope images, cf. Fig. 1(b). The calculated mode overlap Γ with the spin-coated layer of QDs is 7.7% for the TE_{00} mode and 3.2% for the TM_{00} mode. This number allows for a detectable interaction of the optical mode with the QDs. Furthermore, the signal amplitude can be scaled by adapting the propagation length, and the waveguides can be reused for many samples. For applications, the mode overlap with the active region can be increased by using a material with larger refractive index contrast for a better mode confinement or by imbedding the QDs into the waveguide.³⁶ In this case, the overlap will be increased to about 19% and could be increased further by stacking multiple layers of QDs or using a higher refractive index material in the waveguides. With only a factor of two difference to this rather advanced approach, the spin-coating of samples onto a waveguide can be reasonably put forward as the technique of choice for serial testing and characterization experiments.

RESULTS AND DISCUSSION

Figures 4(a) and 4(b) show representative traces of the time-resolved differential transmission in amplitude and phase, respectively, detected by sideband pump-probe spectroscopy with the pump close to the center of the QD luminescence at 1200 nm and the probe tuned from 1200 nm to 1600 nm, well in the QD bandgap [cf. Fig. 1(a)]. The experimental data are shown as solid dots. Note that all pump-probe traces are shown on a logarithmic time scale. For early times, oscillations arising from acoustic noise are visible and are not resolved for later times due to undersampling. The average laser power before the waveguide was $100\ \mu\text{W}$, with an incoupling efficiency of 10%; this equals $10\ \mu\text{W}$ average power or an energy of 150 fJ per pulse. As the repetition rate of the laser exceeds the decay rate of the QD GS exciton of approximately $1\ \mu\text{s}$ by far, we create a quasi-constant GS exciton population.⁴ The transmission and refractive index changes induced by the pump pulse on the picosecond to nanosecond time scale thus reflect not the dynamics of a single GS exciton but rather the interaction of multiple excitations in the system. Throughout the whole investigated range of probe wavelengths, we observe consistently a positive change of the differential transmission, caused by state filling created by the pump pulse on the quasi-static exciton background. The amplitude change is largest at a red detuning of about 50-75 nm from the pump pulse, consistent with

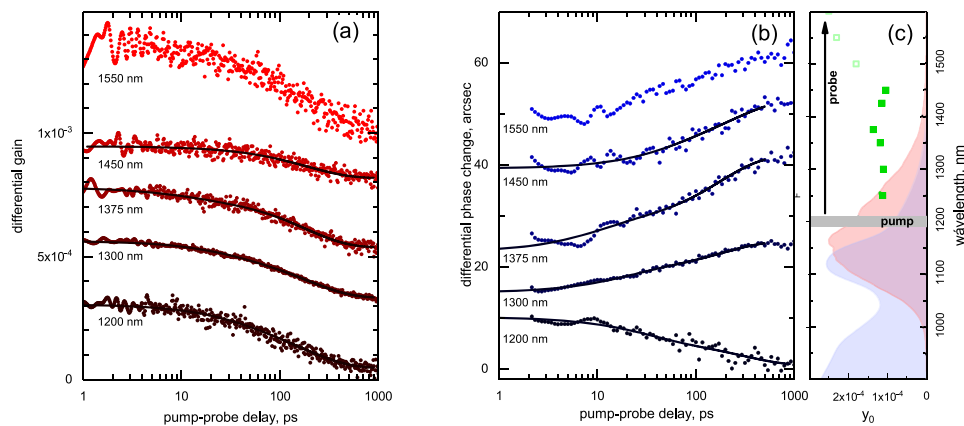


FIG. 4. Differential changes in amplitude (a) and phase (b) in sideband pump-probe experiments with the pump at the maximum of the QD luminescence at 1200 nm and the probe tuned from 1200 nm to 1600 nm. Experimental data are shown as solid dots; the traces are offset for better visibility. The solid lines are biexponential fits of the data. Panel (c) shows the wavelength settings and the offset y_0 in the amplitude as solid (green) squares and for wavelengths longer than 1450 nm as empty squares. Emission and absorption spectra are schematically displayed as shaded red and blue areas, respectively.

the Stark shift expected in this kind of QDs. In the differential phase response, we observe a change in sign between 1200 nm and 1250 nm probe wavelengths, indicative of the crossing of a resonance. This supports the assumption that carriers are created within the GS manifold of the PbS/CdS QDs rather than in an intraband process, as in this case no particular resonance feature is expected. The data taken at 1550 nm and 1600 nm probe wavelengths show a larger noise and artificially higher amplitude, as the probe laser power had to be increased due to decreasing sensitivity of the detector and an exceedingly small diffraction efficiency of the AOM at these long wavelengths. The signature, however, is distinctly positive even at these wavelengths unlike for kHz excitation.¹⁹ This does not exclude the presence of an intraband absorption process; however, this process is not modulated along with the pump modulation under our quasi-cw excitation conditions.

To extract more quantitative information, we fit the traces with a biexponential decay $y(t) = y_0 + A_1 \exp(-t/\tau_1) + A_2 \exp(-t/\tau_2)$, which describes the experimental curves well over three orders of magnitude in time. The data at 1550 nm and 1600 nm probe wavelengths are not fitted because of the signal-to-noise issues mentioned earlier. Also for the phase data taken at 1500 nm probe wavelength, a meaningful fitting was not possible. The fits are shown in the figure as solid lines. The fast and slow time constants are in the range of 30-40 ps and 200 ps, respectively. We did not observe a significant offset in the phase data, while in the amplitude the quasi-static background amounted to up to one quarter of the total signal. The amplitude offset is displayed in Fig. 4(c) together with absorption and emission spectra and the wavelength settings of pump and probe pulses.

Figures 5(a) and 5(b) show exemplary data obtained at pump wavelengths between 1200 nm and 950 nm for a fixed probe wavelength at the QD luminescence maximum at 1200 nm. Again, we observe a consistently positive signal with a maximal amplitude in the response at a blue detuning of 50-75 nm of the pump wavelength with respect to the probe wavelength. At shorter pump wavelengths, the response decreases in amplitude, to reappear at wavelengths shorter than 1000 nm as the excited state continuum of the QDs is addressed. With the low number of carriers created, also the phase response is low between 1200 nm and 1000 nm excitation wavelength. This is also reflected by the variation in magnitude of the quasi-static amplitude offset y_0 displayed in Fig. 5(c).

Biexponential fits of the pump-probe traces are shown in Figs. 5(a) and 5(b) as solid lines. For a range of phase traces, a meaningful fitting of the data was not possible due to an insufficient signal-to-noise ratio at arcsecond phase amplitudes.

In Figs. 6(a) and 6(b), the results of fitting of the pump-probe traces are collected. Figure 6(a) shows a plot of the fast and slow time constants retrieved from the probe and pump wavelength series as red squares and blue circles, respectively. Independent of the wavelength combination, we observe a two-component decay with the fast time constant in the range of 30-40 ps and the slow time

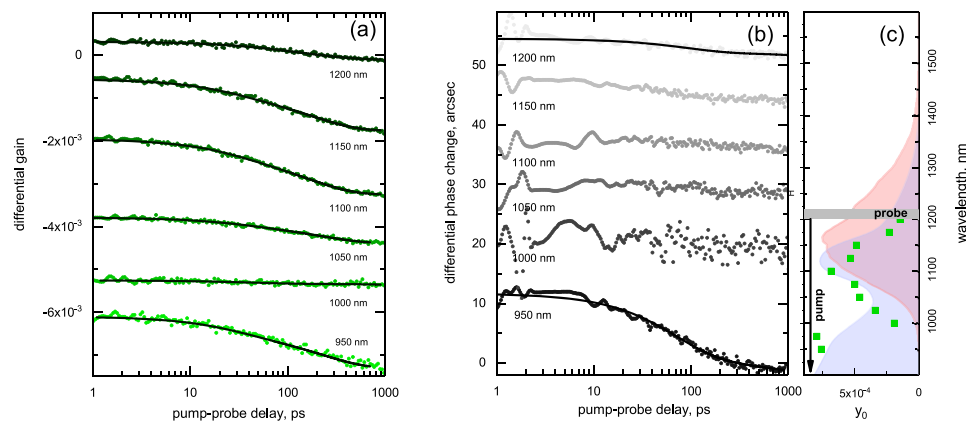


FIG. 5. Differential changes in amplitude (a) and phase (b) in sideband pump-probe experiments with the probe at the maximum of the QD luminescence at 1200 nm and the pump tuned from 1200 nm into the excited state continuum at 950 nm. Experimental data are shown as solid dots; the traces are offset for better visibility. The solid lines are biexponential fits of the data. Panel (c) shows the wavelength settings and the offset y_0 in the amplitude as solid (green) squares. Emission and absorption spectra are schematically displayed as shaded red and blue areas, respectively.

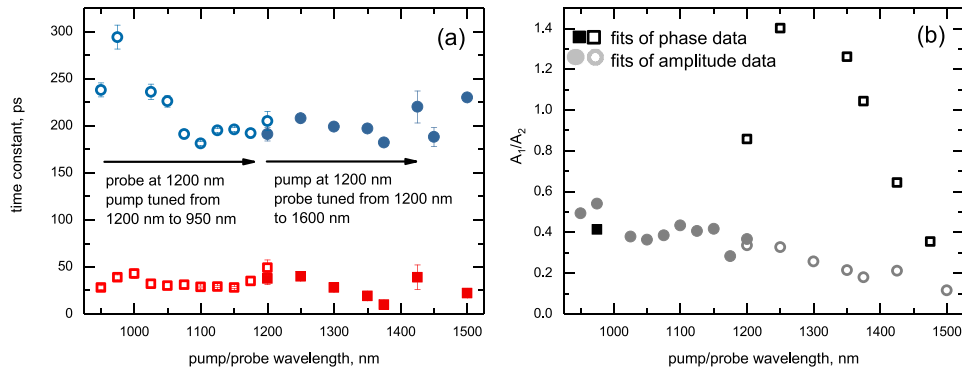


FIG. 6. (a) Slow and fast time constants extracted by biexponential fits of the amplitude data. Open symbols represent values extracted from the pump wavelength series; solid symbols represent values from the probe wavelength series. (b) Amplitude ratios of fast to slow components from the fits shown in Figs. 4 and 5. Circles represent the amplitude ratios as derived from fitting the differential amplitude change; squares represent the amplitude ratios derived from fitting the differential phase change.

constant of about 200 ps. We attribute the fast decay time as a relaxation of the exciton system via Auger processes (40 ps). The time we observe agrees excellently with the size-dependent nonradiative Auger rates for PbS QDs found in Ref. 44. The slow decay time is in the range of times observed for the biexciton decay in PbS QDs,^{20,25} after which the original quasi-equilibrium population of excitons is restored. The number of excitons created per dot can be calculated from the energy per pulse ($E_p \approx 150$ fJ), the photon energy E_{hv} , the absorption cross section $\sigma_{\text{abs},\lambda_{\text{pump}}}$ of a quantum dot at the pump wavelength, the mode confinement Γ , and the mode area A_{mode} ,

$$\langle N \rangle \approx \frac{E_p}{E_{hv}} \times \frac{\Gamma}{A_{\text{mode}}} \times \sigma_{\text{abs},\lambda_{\text{pump}}} \times \frac{2\nu_{\text{rep}}}{k_r}. \quad (3)$$

We assume a pump wavelength of 900 nm, a mode area of $2 \mu\text{m}^2$, and $\Gamma = 7.7\%$, see Fig. 3(c). The absorption cross section at the pump wavelength can be calculated from the intrinsic absorption coefficient³ and is about $2 \times 10^{-15} \text{ cm}^2$ for our dots at 900 nm. Using the formalism proposed in Ref. 4, the radiative rate k_r is estimated as 0.6 MHz. This yields an average number of excitons created of $\langle N \rangle \approx 0.66$. Assuming Poisson statistics for the population of the QDs,⁴⁵ the probability of a biexciton to occur is 11%, and thus the slow decay component can reasonably be attributed to biexciton decays.

Figure 6(b) shows the ratio of the amplitudes A_1 and A_2 of the fast and the slow decay components, respectively. In the differential transmission traces, we observe a larger contribution of the slow biexciton decay component to the total signal, while this relation is reversed in the differential phase change data. This confirms the hypothesis that the fast process is a thermalization process, as hot carriers and unpaired electrons and holes cause intraband transitions with a significant contribution to the refractive index.⁴⁶ The time constant of the process differs significantly from the relaxation time of carriers created with a large excess energy in the absorption continuum of the PbS/CdS QD. For these conditions, relaxation times in the QD GS as short as 2 ps have been reported.^{19,47} With our quasi-resonant excitation with very little excess energy, the process dominating the carrier dynamics is an energetic rearrangement with the GS exciton manifold of the QDs.

CONCLUSIONS

We have investigated the response of PbS/CdS quantum dots coupled to a silicon nitride waveguide to an optical excitation at high repetition rates. In order to resolve the small modulation in population and refractive index induced by an excitation with a frequency much higher than the GS exciton decay rate, we developed a side-band heterodyne pump-probe approach, which allows us to detect very small changes in amplitude and phase of the probe pulse by a drift-resistant self-referencing approach. Pumping and probing across the QD GS absorption and emission band, we

consistently observe an absorption bleach, which recovers with a fast time constant and a slow time constant of 40 ps and 200 ps, respectively. These processes are attributed to exciton thermalization and biexciton decay, respectively. To push the limits for the application of the PbS/CdS material system in fast telecommunications, our results suggest a route for further investigations. In particular, it is desirable to dramatically shorten the GS lifetime of the used nanostructures. A most promising development in this direction is the establishment of colloidal nanostructures with two-dimensional confinement, so-called nanoplatelets, which show a greatly reduced GS exciton lifetime compared to QDs.⁴⁸ To enhance the modulation depth reached in photonic devices, the QDs or nanoplatelets can be implanted into the silicon nitride waveguide, as has been demonstrated in Ref. 36.

The sideband pump-probe method we developed proved to be a suitable tool for the quantitative measurement of small changes in the imaginary and real parts of the refractive index. In differential measurements, we were able to resolve changes of the order of 10^{-5} in amplitude and phase, reaching a sensitivity which is only equalled by the phase-insensitive double chop pump-probe approach. Using waveguides to enhance the overlap of pump and probe beams and the sample under investigation provides a route to further enhance the signal-to-noise ratio in experiments.

ACKNOWLEDGMENTS

Funding was provided by Deutsche Forschungsgemeinschaft via CRC 787 and the GRK 1558. This work is partly supported by the EU through the projects ERC-ULPPIC, ITN Phonsi and by the Belgian Science Policy Office (IAP). P.G. acknowledges the support by FWO-Vlaanderen. A.W.A. acknowledges funding from Deutsche Forschungsgemeinschaft via Grant No. AC290-2/1. Singh and Li at UT-Austin were supported by NSF DMR-1306878. Li also gratefully acknowledges the support from a Humboldt fellowship, which facilitated the collaboration with TU Berlin.

- ¹ A. P. Alivisatos, *Science* **271**, 933–937 (1996).
- ² U. Woggon, *Optical Properties of Semiconductor Quantum Dots*, Springer Tracts in Modern Physics Vol. 137 (Springer, 1997).
- ³ I. Moreels, K. Lambert, D. Smeets, D. D. Muynck, T. Nollet, J. C. Martins, F. Vanhaecke, A. Vantomme, C. Delerue, G. Allan, and Z. Hens, *ACS Nano* **3**, 3023–3030 (2009).
- ⁴ Y. Justo, P. Geiregat, K. van Hoecke, F. Vanhaecke, C. de Mello Donega, and Z. Hens, *J. Phys. Chem. C* **117**, 20171–20177 (2013).
- ⁵ F. Masia, W. Langbein, I. Moreels, Z. Hens, and P. Borri, *Phys. Rev. B* **83**, 201309(R) (2011).
- ⁶ F. Masia, N. Accanto, W. Langbein, and P. Borri, *Phys. Rev. Lett.* **108**, 087401 (2012).
- ⁷ S. Gaponenko, H. V. Demir, C. Seassal, and U. Woggon, *Opt. Express* **24**, A430–A433 (2016).
- ⁸ Y. Shirasaki, G. J. Supran, M. G. Bawendi, and V. Bulović, *Nat. Photonics* **7**, 13–23 (2013).
- ⁹ F. Fan, O. Voznyy, R. P. Sabatini, K. T. Bicanic, M. M. Adachi, J. R. McBride, K. R. Reid, Y.-S. Park, X. Li, A. Jain, R. Quinteros-Bermudez, M. Saravanapavanantham, M. Liu, M. Korkusinski, P. Hawrylak, V. I. Klimov, S. J. Rosenthal, S. Hoogland, and E. H. Sargent, *Nature* **544**, 75–79 (2017).
- ¹⁰ W. Xie, T. Stöferle, G. Rainò, T. Aubert, S. Bisschop, Y. Zhu, R. F. Mahrt, P. Geiregat, E. Brainis, Z. Hens, and D. van Thourhout, *Adv. Mater.* **29**, 1604866 (2017).
- ¹¹ J.-C. Weeber, K. Hammami, G. C. de Francs, A. Bouhelier, J. Arocas, A. Kumar, F. Eloi, S. Buil, X. Quélin, J.-P. Hermier, M. Nasilowski, and B. Dubertret, *ACS Photonics* **3**, 844–852 (2016).
- ¹² D. V. Talapin, J.-S. Lee, M. V. Kovalenko, and E. V. Shevchenko, *Chem. Rev.* **110**, 389–458 (2010).
- ¹³ K.-S. Chi, E. K. Lee, W.-J. Joo, E. Jang, T.-H. Kim, S. J. Lee, S.-J. Kwon, J. Y. Han, B.-K. Kim, B. L. Choi, and J. M. Kim, *Nat. Photonics* **3**, 341–345 (2009).
- ¹⁴ P. Wolf, P. Moser, G. Larisch, H. Li, J. A. Lott, and D. Bimberg, *Electron. Lett.* **49**, 666–667 (2013).
- ¹⁵ R. S. Tucker and K. Hinton, *IEEE Photonics J.* **3**, 821–833 (2011).
- ¹⁶ K. Nozaki, T. Tanabe, A. Shinya, S. Matsuo, T. Sato, H. Taniyama, and M. Notomi, *Nat. Photonics* **4**, 477–483 (2010).
- ¹⁷ S. L. Chuang, *Physics of Photonic Devices* (Wiley, 2009).
- ¹⁸ P. Kambhampati, *J. Phys. Chem. Lett.* **3**, 1182–1190 (2012).
- ¹⁹ P. Geiregat, A. J. Houtepen, D. van Thourhout, and Z. Hens, *ACS Nano* **10**, 1265–1272 (2015).
- ²⁰ A. Omari, I. Moreels, F. Masia, W. Langbein, P. Borri, D. van Thourhout, P. Krockaert, and Z. Hens, *Phys. Rev. B* **85**, 115318 (2012).
- ²¹ N. Accanto, F. Masia, I. Moreels, Z. Hens, W. Langbein, and P. Borri, *ACS Nano* **6**, 5227–5233 (2012).
- ²² R. Scott, A. W. Achtstein, A. Prudnikau, A. Antanovich, S. Christodoulou, I. Moreels, M. Artemyev, and U. Woggon, *Nano Lett.* **15**, 4985–4992 (2015).
- ²³ R. D. Schaller and V. I. Klimov, *Phys. Rev. Lett.* **92**, 186601 (2004).
- ²⁴ R. J. Ellingson, M. C. Beard, J. C. Johnson, P. Yu, O. I. Micic, A. J. Nozik, A. Shabaev, and A. L. Efros, *Nano Lett.* **5**, 865–871 (2005).
- ²⁵ B. de Geyter, A. J. Houtepen, S. Carrillo, P. Geiregat, Y. Gao, S. ten Cate, J. M. Schins, D. van Thourhout, C. Delerue, L. D. A. Siebbeles, and Z. Hens, *ACS Nano* **6**, 6067–6074 (2012).

- ²⁶ P. Reiss, M. Protière, and L. Li, *Small* **5**, 154–168 (2009).
- ²⁷ M. P. Hendricks, M. P. Campos, G. T. Cleveland, I. J.-L. Plante, and J. S. Owen, *Science* **348**, 1226–1230 (2015).
- ²⁸ J. M. Pietryga, D. J. Werder, D. J. Williams, J. L. Casson, R. D. Schaller, V. I. Klimov, and J. A. Hollingsworth, *J. Am. Chem. Soc.* **130**, 4879–4885 (2008).
- ²⁹ S. Romero-Garcia, F. Merget, F. Zhong, H. Finkelstein, and J. Witzens, *Opt. Express* **21**, 14036–14046 (2013).
- ³⁰ M. Melchiorri, N. Daldosso, F. Sbrana, L. Pavesi, G. Pucker, C. Kompocholis, P. Bellutti, and A. Liu, *Appl. Phys. Lett.* **86**, 121111 (2005).
- ³¹ J. F. Bauters, M. J. R. Heck, D. John, D. Dai, M.-C. Tien, J. S. Barton, A. Leinse, R. G. Heideman, D. J. Blumenthal, and J. E. Bowers, *Opt. Express* **19**, 3163–3174 (2011).
- ³² M. W. McCutcheon and M. Lončar, *Opt. Express* **16**, 19136–19145 (2008).
- ³³ F. B. Arango, A. Kwadrin, and A. F. Koenderink, *ACS Nano* **6**, 10156–10167 (2012).
- ³⁴ N. Gruhler, C. Benz, H. Jang, J.-H. Ahn, R. Danneau, and W. H. P. Pernice, *Opt. Express* **21**, 31678–31689 (2013).
- ³⁵ P. Purnawirman, J. Sun, T. N. Adam, G. Leake, D. Coolbaugh, J. D. B. Bradley, E. S. Hosseini, and M. R. Watts, *Opt. Lett.* **38**, 1760–1762 (2013).
- ³⁶ W. Xie, Y. Zhu, T. Auber, S. Verstuyft, Z. Hens, and D. van Thourhout, *Opt. Express* **23**, 12152–12160 (2015).
- ³⁷ E. Murray, D. J. P. Ellis, T. Meany, F. F. Floether, J. P. Lee, J. P. Griffiths, G. A. C. Jones, I. Farrer, D. A. Ritchie, A. J. Bennett, and A. J. Shields, *Appl. Phys. Lett.* **107**, 171108 (2015).
- ³⁸ K. Ikeda, R. E. Saperstein, N. Alic, and Y. Fainman, *Opt. Express* **16**, 12987–12994 (2008).
- ³⁹ A. Omari, P. Geiregat, D. van Thourhout, and Z. Hens, *Opt. Express* **21**, 23272–23285 (2013).
- ⁴⁰ P. Borri, W. Langbein, J. Mørk, and J. Hvam, “Heterodyne pump-probe and four-wave mixing in semiconductor optical amplifiers using balanced lock-in detection,” *Opt. Commun.* **169**, 317–324 (1999).
- ⁴¹ M. Kolarczik, N. Owschimikow, B. Herzog, F. Buchholz, Y. I. Kaptan, and U. Woggon, *Phys. Rev. B* **91**, 235310 (2015).
- ⁴² F. Masia, W. Langbein, and P. Borri, *Phys. Rev. B* **85**, 235403 (2012).
- ⁴³ R. J. Suess, M. M. Jadidi, K. Kim, and T. E. Murphy, *Opt. Express* **22**, 17466–17477 (2014).
- ⁴⁴ A. O. El-Ballouli, E. Alarousu, A. Usman, J. Pan, O. M. Bakr, and O. F. Mohammed, *ACS Photonics* **1**, 285–292 (2014).
- ⁴⁵ R. D. Schaller and V. I. Klimov, *Phys. Rev. Lett.* **96**, 097402 (2006).
- ⁴⁶ B. Herzog, B. Lingnau, M. Kolarczik, Y. Kaptan, D. Bimberg, A. Maaßdorf, U. W. Pohl, R. Rosales, J.-H. Schulze, A. Strittmatter, M. Weyers, U. Woggon, K. Lüdge, and N. Owschimikow, *Appl. Phys. Lett.* **109**, 201102 (2016).
- ⁴⁷ F. Masia, I. Moreels, Z. Hens, W. Langbein, and P. Borri, *Phys. Rev. B* **82**, 155302 (2010).
- ⁴⁸ A. W. Achtstein, R. Scott, S. Kickhöfel, S. T. Jagsch, S. Christodoulou, G. H. V. Bertrand, A. V. Prudnikau, A. Antanovich, M. Artemyev, I. Moreels, A. Schliwa, and U. Woggon, *Phys. Rev. Lett.* **116**, 116802 (2016).